Phase-Transition-Enhanced Thermoelectric Transport in Rickardite Mineral Cu3– xTe2

Mujde Yahyaoglu, Melis Ozen, Yurii Prots, Oussama El Hamouli, Vahe Tshitoyan, Huiwen Ji, Ulrich Burkhardt, Bertrand Lenoir, G. Jeffrey Snyder, Anubhav Jain, et al.

Phase-Transition-Enhanced Thermoelectric Transport in Rickardite Mineral $Cu_{3-x}Te_2$

Mujde Yahyaoglu,[†,‡] Melis Ozen,[†,‡] Yurii Prots,[§] Oussama El Hamouli,[⊥] Vahe Tshitoyan,[ξ] Huiwen Ji,[ξ] Ulrich Burkhardt,[§] Bertrand Lenoir,[⊥] G. Jeffrey Snyder,[δ] Anubhav Jain,[ξ] Christophe Candolfi,[⊥] and Umut Aydemir[*,‡,ϕ]

[†] Graduate School of Sciences and Engineering, Koç University, Sariyer, Istanbul-34450, Turkey
[‡] Koç University Boron and Advanced Materials Application and Research Center (KUBAM), Sariyer, Istanbul-34450, Turkey
[§] Max-Planck-Institut für Chemische Physik fester Stoffe, Dresden-01187, Germany
[⊥] Institut Jean Lamour, Université de Lorraine, Nancy Cedex-54011, France
[ξ] Energy Technologies Area, Lawrence Berkeley National Lab, Berkeley, CA-94720, USA
[δ] Department of Materials Science and Engineering, Northwestern University, Evanston, IL-60208, USA
[ϕ] Department of Chemistry, Koç University, Sariyer, Istanbul-34450, Turkey
* Email: uaydemir@ku.edu.tr

ABSTRACT: The binary copper chalcogenides $Cu_{2-\delta}X$ (X = S, Se, and Te) have recently gained significant interest due to their high thermoelectric performance at moderate temperatures. In an effort to unveil new Cu-based compounds with promising thermoelectric potential, $Cu_{3-x}Te_2$ rickardite mineral emerged as a candidate based on a purely text mining approach applied by a machine learning method. Polycrystalline samples of $Cu_{3-x}Te_2$ within the homogeneity range (x = 0.1, 0.2) were successfully synthesized from the raw elements by a solid-state method. High-temperature powder X-ray diffraction combined with differential scanning calorimetry and specific heat measurements showed several reversible phase transitions at around 458 K, 640 K, and 647 K. Signatures of these transitions were observed on the electronic and thermal transport properties, measured over a broad range of temperatures (5 – 733 K). The transition undergone by this compound at 647 K results in a crossover from metallic-like to semiconducting-like properties. The combination of high-power factor and low thermal conductivity in the high-temperature phase results in improved thermoelectric performances with a peak dimensionless thermoelectric figure of merit zT of ~ 0.14 at 733 K. The synthetic rickardite mineral is an exciting candidate to be used as a phase change material in broad application areas such as in waste heat harvesting and photovoltaic systems.

INTRODUCTION

Developing sustainable and environmentally friendly energy conversion technologies is a key challenge to overcome the impending energy crisis. Thermoelectric (TE) materials may play an important role in the clean and sustainable energy solution landscape by converting waste heat into electricity and serving as vibration- and noise-free solid-state coolers because of their high reliability without hazardous gas emissions[1]. The thermoelectric efficiency of a material is determined by the dimensionless thermoelectric figure of merit, $zT = \alpha^2T/\rho\kappa$, where α, T, ρ and κ are the Seebeck coefficient (or thermopower), absolute temperature, electrical resistivity, and total thermal conductivity, respectively.[1] Because these transport parameters are interdependent to each other, the phonon-glass electron-crystal (PGEC) concept has been proposed as a possible route to enhancing zT by decoupling these transport parameters. In PGEC materials, structural disorder is desired for achieving low lattice thermal conductivity (phonon-glass) while retaining its crystalline nature for good electronic transport properties (electron-crystal), maximizing the power factor (α^2/ρ).[2] A fruitful strategy to design such a PGEC material is to seek for crystal structures that can be viewed as two sublattices: one composed of an electrically-conducting network while the other behaves as a thermal blocker.

Owing to these decoupled transport properties[3, 4], copper chalcogenides including liquid-like materials (superionic semiconductors)[5-22], diamond-like compounds[23-27], and layered-structure compounds[28-34] have all recently gained significant attention as promising thermoelectric materials[4]. Cu-based chalcogenides show an intriguing thermal transport stemming from the mobile Cu ions introducing additional scattering centers, thus, shortening the phonon mean free path[3].

Many studies on binary and ternary Cu-based materials can be found in the literature e.g., $Cu_{2-\delta}X$ (X = S, Se, and

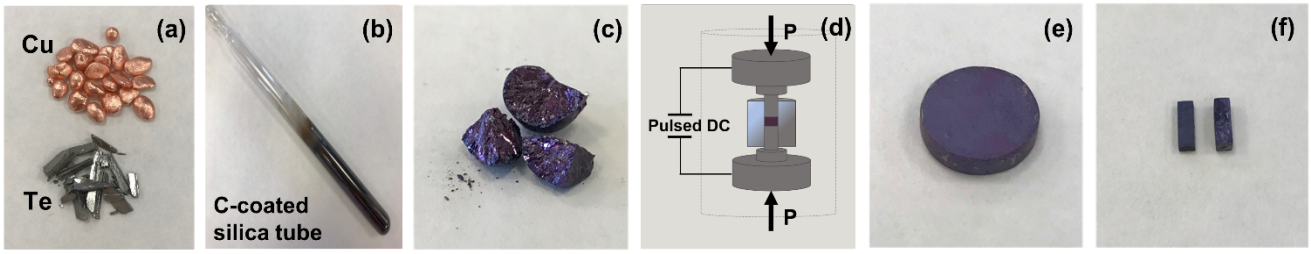

Figure 1. Synthesis and sample preparation procedures of $Cu_{2.8}Te_2$ and $Cu_{2.9}Te_2$, a) raw materials of Cu and Te, b) C-coated silica tube used for annealing, c) synthesized $Cu_{2.9}Te_2$, d) schematic representation of sintering (SPS) process, e) dense pellets obtained after SPS for thermal transport measurements, f) samples cut for electrical transport measurements.

Te)[5-7, 10-16], Cu_8GeSe_6[17], Cu_5FeS_4[18], Cu_7PSe_6[19], $CuCrSe_2$[20], CuAgSe[21], $CuCrS_2$[22], etc. In $Cu_{2-\delta}X$ (X = S, Se, and Te), rigid sublattices formed by X atoms provide a crystalline pathway for conducting carriers while disordered Cu atoms with high diffusivity (on the order of 10^{-5} cm^2/s) jump sequentially between equilibrium positions[3]. At high temperatures, the Cu_2X phases possess disordered cubic structures, while they have complex crystal structures at lower temperatures[4]. Stoichiometric compounds such as Cu_2Se and Cu_2S undergo one- and two-phase transitions, respectively. The structural complexity of the Cu_2Te phase is evidenced by the sequential appearance of five phase transitions until a final f.c.c. structure is reached[4]. In addition to stoichiometric Cu_2X compounds, many Cu-deficient variants ($Cu_{2-\delta}X$) have been reported[5-7, 12]. Although the structural complexity further increases upon varying the Cu/X ratio, introducing Cu-deficiency tunes the hole concentration to the optimal value yielding high thermoelectric performance. The fact that Cu-X bonding becomes less polar and weaker from S over Se to Te, Cu deficiencies are more prone to form, leading to high carrier concentrations. Moreover, the lattice thermal conductivity of tellurides is lower than that of selenides or sulfides due to the larger atomic size of Te and weaker Cu-X bonds[4].

In an effort to explore other Cu-based binary compounds, we report on a detailed investigation of the crystal structure and thermoelectric properties over a broad range of temperatures (5 – 733 K) of the binary compound $Cu_{3-x}Te_2$. Our experimental study was guided by a machine learning method based on information-dense word (e.g, thermoelectric, zT or thermopower) embedded in scientific abstracts. This method enables predicting new potential thermoelectric materials[35, 36], as validated (in part) by comparing the predicted thermoelectric compositions with available computational data sets[37] as well as experimental power factors and zT values[38]. $Cu_{3-x}Te_2$ is a naturally occurring mineral known as rickardite with poorly reported structural, chemical and transport properties[39-43]. Motivated by the high thermoelectric performance and potential of commercialization due to low production costs of Cu-based minerals such as $Cu_{2-\delta}S$[6], $Cu_{26}V_2Ge_6S_{32}$ (colusite)[44], $Cu_{12}Sb_4S_{13}$ (tetrahedrite)[45], and Cu_5FeS_4 (bornite)[18], we investigated the transport properties of synthetic rickardite mineral. In agreement with the complex binary phase diagram of Cu-Te[46] (Figure S1), several reversible phase transitions were evidenced by differential scanning calorimetry and specific heat measurements at around 458, 640 and 647 K. While the first transition has little influence on the transport properties, the high-temperature transitions lead to a metal-insulator-like transition marked by a steep rise in the electrical resistivity and thermopower values and a sharp drop in the thermal conductivity values. Because of more favorable electronic and thermal properties, the high-temperature phase shows better thermoelectric performance resulting in a moderate zT value of ~0.14 at 733 K.

EXPERIMENTAL METHODS

Sample Preparation. Copper beads (Cu, Sigma Aldrich > 99.99 % metal basis) and tellurium pieces (Te, Alfa Aesar 99.9999 % metals basis) were used as starting materials to synthesize polycrystalline $Cu_{3-x}Te_2$ samples. To remove surface oxides, copper beads were put inside an alumina holder, placed in a quartz tube, and kept at 773 K under H_2/Ar flow for 4 hours. Afterward, $Cu_{3-x}Te_2$ samples were synthesized by reacting cleaned copper and tellurium in stoichiometric ratio of $Cu_{2.8}Te_2$ and $Cu_{2.9}Te_2$ by a solid-state synthesis method. Raw materials were sealed into a carbon-coated silica tube under vacuum. The sealed tube was then placed into muffin furnace and kept at 1223 K for 12 hours. After quenching in water at room-temperature, the tube was put into a preheated furnace for further annealing at 623 K for 96 hours. The final product has shining purple color appearance, similar to that reported in the literature for $Cu_{3-x}Te_2$[40] (Figure 1). For chemical characterizations and transport property measurements, dense cylindrical pellets were obtained by spark plasma sintering (SPS; Syntex Inc., Dr Sinter 515S model) in a graphite die at 623 K for 10 minutes under a pressure of 65 MPa. The densities of the samples were calculated to be 7.35 g/cm^3 and 7.43 g/cm^3 for $Cu_{2.8}Te_2$ and $Cu_{2.9}Te_2$, respectively, from geometrical dimensions and weight of the consolidated pellets. Considering the crystallographic density of the phase $Cu_{2.8}Te_2$ with 7.54 g/cm^3,[40] the relative densities amount 97 % and 99 %, respectively. Based on these results, we consider that the transport data collected on SPS treated samples give reliable intrinsic behavior of the rickardite phase.

Sample Characterization. Single crystal X-ray diffraction (XRD) data was collected with a Rigaku AFC7 diffractometer (MoKα radiation, λ = 0.71073 Å) equipped with a Saturn 724+ CCD detector. The phase purity of samples was analyzed by using Rigaku MiniFlex 600 (Cu Kα = 1.5418 Å, 40 kV voltage, and 15 mA) and Huber Guinier G670 Camera (CuKα_1 radiation = 1.54056 Å). The structure refinements as well as the lattice parameters and crystallographic calculations were performed with the WinCSD program package[47]. High-temperature XRD (HTXRD) measurements were carried out in sealed glass capillaries with a high-temperature stage attached in STOE STADI-MP diffractometer (Mo Kα = 0.71073 Å). Microstructure analyses were realized using Scanning Electron Microscope (SEM Jeol JSM 7800F Field Emissioncathode) equipped with EDX system and optical Microscope (OM, Zeiss Axioplan 2) techniques. The target phases' chemical compositions were determined by electron microprobe analysis using wavelength dispersive X-ray spectroscopy (WDS, Cameca SX 100, tungsten cathode). The phase transition temperatures were determined by Differential Scanning Calorimetry (DSC, Netzsch STA 449 F3 Jupiter) measurements. Heat capacity, C_p, measurements were carried out under N_2 flow via the ratio method using the same DSC instrument with a heating rate of 10 K min^{-1} and using sapphire as standard material. To determine the speed of phase transitions, additional C_p measurement (calculated according to DIN 51007) was performed using a DSC apparatus (Netzsch 403 F3) with a heating rate of 20 K min^{-1} and using sapphire as standard material.

Transport Property Measurements. Electrical and thermal transport properties were measured between 5 and 733 K on polycrystalline dense samples cut with a diamond-wire saw into appropriate shape and dimensions. Low-temperature measurements (5 – 300 K) of the electrical resistivity, Seebeck coefficient and thermal conductivity measurements were carried out on a bar-shaped sample with the thermal transport option (TTO) of a physical property measurement system (PPMS, Quantum Design, San Diego, CA, USA). Four copper leads were brazed onto the sample using a low-melting-point braze. Hall effect measurements were performed on the same sample using the AC transport option of the PPMS. A five-probe configuration was used by brazing five copper wires onto the sample with a low-melting-point braze. The transverse electrical resistivity ρ_{xy} was measured by sweeping the magnetic field $\mu_0 H$ between –1 and +1T. The Hall resistivity ρ_H was calculated following the formula $\rho_H = [\rho_{xy}(+\mu_0 H) - \rho_{xy}(-\mu_0 H)]/2$ to dismiss possible magnetoresistive contributions. The Hall charge carrier concentration n_H and Hall mobility μ_H were inferred from the single-band formulas $n_H = -1/R_H e$ and $\mu_H = R_H/\rho$ where e is the elementary charge and R_H is the Hall coefficient determined from the slope of the $\rho_H(\mu_0 H)$ data for $\mu_0 H \to 0$. Specific heat measurement was performed under zero magnetic field on a small dense piece of approximately 20 mg using the ^{4}He specific heat option of the PPMS. The piece was glued onto the platform of the sample holder by using a minute amount of Apiezon N grease to ensure a good thermal contact between the sample and the platform. The low-temperature transport property data can be found in the Supporting Information file.

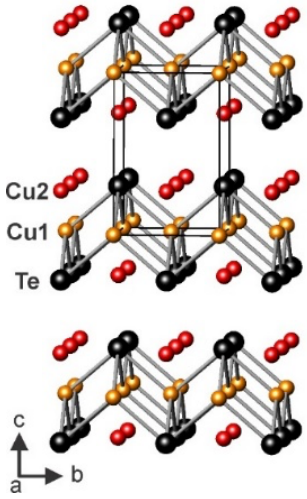

Figure 2. Crystal structure of $Cu_{2.8}Te_2$. The ordered part of the structure (Cu1 and Te atoms) is emphasized as Cu–Te framework with d(Cu–Te) = 2.6313(9) Å and 2.6625(9) Å, the partially occupied Cu2 position (occupancy factor 0.406(1)) are represented as individual atoms.

At high temperatures (300 – 733 K), the thermal conductivity was measured on a disc-shaped cylindrical pellet. Measurements of the thermal diffusivity, D, were carried out using a Netzsch LFA HT467 laser flash apparatus. Thermal conductivity of the samples was calculated using the relation: $\kappa = DC_P d$, where C_P is the experimentally heat capacity measured by DSC and d is the experimental density. High-temperature electrical resistivity and thermopower measurements were performed using a ZEM-3 measurement system (Ulvac-Riko, Japan) on a bar-shaped sample. Magnetization curves $M(\mu_0 H)$ were measured between 300 and 680 K using a high-temperature vibrating sample magnetometer (VSM, MicroSense) under magnetic fields, $\mu_0 H$ of up to 0.5 T. A polycrystalline piece of ~26 mg was glued onto a silica sample holder using a small amount of non-magnetic ceramic paste. The magnetic susceptibility, χ was inferred from the slope of the $M(\mu_0 H)$ curves, which were found to be linear in the temperature and magnetic field ranges covered.

RESULTS AND DISCUSSION

Crystal Structure. Rickardite mineral differs from other copper tellurides both in composition and appearance due to its characteristic purple color. Because of its uncertain composition and unknown crystal structure, rickardite was first recognized as weissite, $Cu_{2-x}Te$[48]. Both minerals are massive with approximately the same hardness but differ in density and color, suggesting different electronic properties at room temperature. Following detailed studies of

the binary Cu-Te system and rickardite phase[40, 49], the structural formula was reported as $Cu_{4-x}Te_2$ indicating Cu deficiency of approximately one atom per unit cell. Rickardite displays an unconventional defective structure with a large amount of vacant metal positions. These prior investigations have clearly confirmed that rickardite is distinct from the slightly Cu-deficient weissite phase, $Cu_{2-x}Te$[40, 49].

To determine the atomic arrangements, the search for analogous structures revealed that copper antimonide (Cu_2Sb) determined by Elander, Hägg and Westgren is structurally similar to rickardite[50]. The crystal structures of both compounds were described in the space group $P4/nmm$ with lattice parameters a = 3.97 Å, c = 6.11 Å and a = 3.992 Å, c = 6.091 Å for the rickardite and copper antimonide, respectively. Both compounds have a similar atomic arrangement (isostructural) and a layered crystal structure in which close-packed layers are weakly bound to Te atoms by half-filled Cu positions[40].

For $Cu_{3-x}Te_2$, both orthorhombic[49] and tetragonal[39] symmetries were reported. Herein, the crystal structure of this compound was investigated by single-crystal X-ray diffraction. From the obtained experimental data, the orthorhombic and tetragonal structures could not be unambiguously distinguished due to very close lattice parameters a and b, as well as very similar agreement of the refinement factors, that is R_{int} values, for Laue symmetries mmm and $4/mmm$. However, clear splitting of the respective reflections was observed on the PXRD patterns indicating an orthorhombic lattice symmetry. A specific set of weak reflections, both on single-crystal and powder diffraction data, was also observed, suggesting that the crystal structure of $Cu_{3-x}Te_2$ is modulated (The detailed report about the investigation of the modulated model of the structure will be a subject of a separate publication). Moreover, single crystalline specimens show a tendency to form twinned agglomerates, which will require further investigations. Hereafter, a subcell in the orthorhombic space group $Pmmn$ will be used for the description of the room-temperature crystal structure of $Cu_{3-x}Te_2$. Tellurium and copper atoms are distributed on one and two crystallographic sites, respectively (Figure 2). One copper position (Cu1 at the 2a site) is fully occupied, while the second (Cu2 at the 2b site) is partially occupied. The ordered part of the structure of $Cu_{3-x}Te_2$, the Te subcell and planar arrangements of Cu atoms, reproduce an atomic arrangement found in the tetragonal FeS (PbO) structure (space group $P4/nmm$). This structure type is typically observed for equiatomic phases described in the binary transition metal–Te (Se) systems, e.g., FeTe[51], FeSe[52], mixed (Fe,Cu)Se[53]. Interestingly, in contrast, the CuTe phase exhibits a corrugated (not planar) Cu sublattice in the space group $Pmmn$[51].

The XRD results of the samples are shown in Figure 3 demonstrating that the target phase has been obtained successfully with a minute amount of CuTe as a secondary phase. With increasing nominal copper content (x = 0.1),

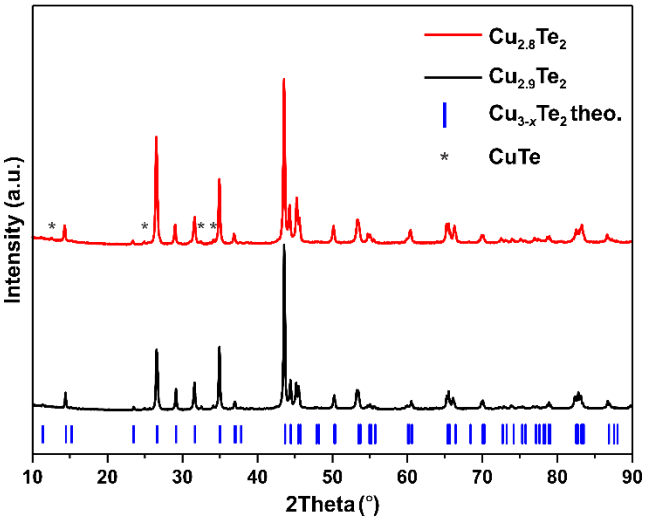

Figure 3. XRD patterns (Cu Kα) of experimental $Cu_{2.8}Te_2$ (red) and $Cu_{2.9}Te_2$ (black) after SPS. The ticks mark the theoretical peak positions of the low temperature phase of $Cu_{3-x}Te_2$.

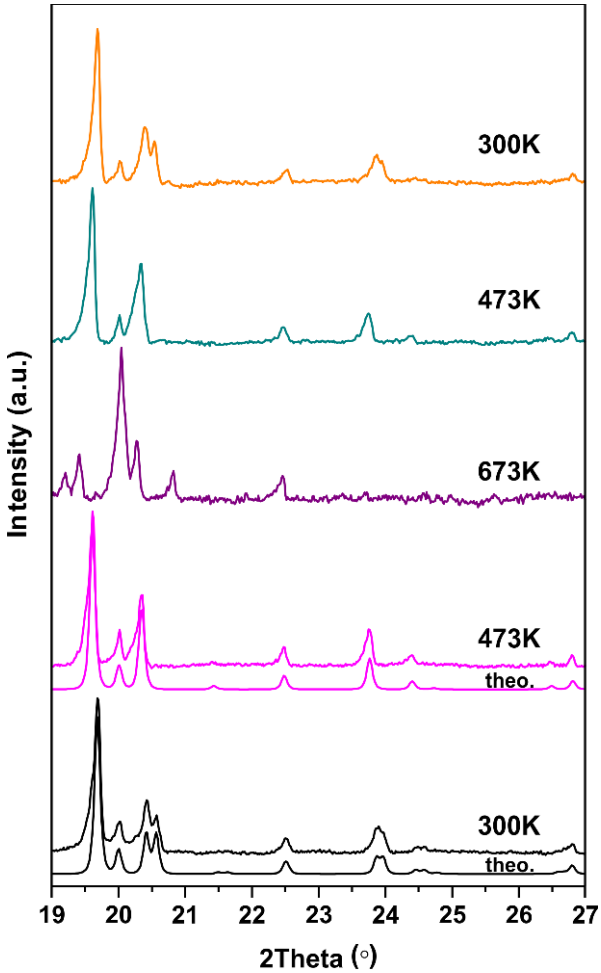

Figure 4. HT-XRD patterns (Mo Kα) of a $Cu_{2.8}Te_2$ sample at 300 K, 473 K, and 673 K upon heating and cooling (theoretical peak positions for orthorhombic (black) and tetragonal (pink) phases are given below the experimental data).

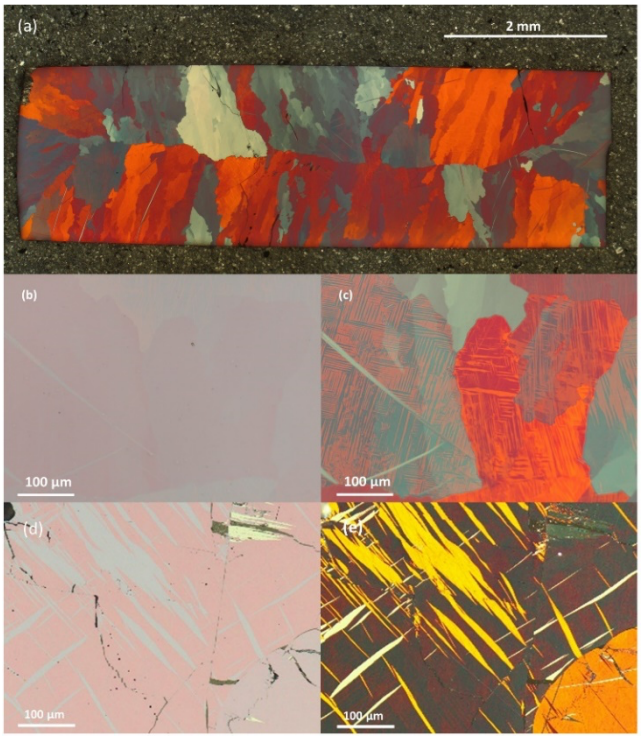

Figure 5. Optical microscopy images of rickardite samples; a) bulk piece under polarized light, b) zoomed version of bulk piece under bright field, and c) polarized light of $Cu_{2.8}Te_2$. d) The bright field and e) polarized light images of $Cu_{2.9}Te_2$.

the amount of CuTe is suppressed slightly. The lattice parameters of the two products were found to be a = 3.9933(1), b = 3.9635(1), c = 6.1159(3) Å for $Cu_{2.8}Te_2$ and a = 4.0067(2), b = 3.9793(2), c = 6.1120(3) Å for $Cu_{2.9}Te_2$. The slight increase in a and b and decrease in c lattice parameters for the latter case can be correlated with its fewer Cu vacancies (Cu2 occupancy: 0.422(9) and 0.446(7), respectively) (see Table S1 and S2 for $Cu_{2.9}Te_2$).

High-temperature XRD measurements were performed on a $Cu_{2.8}Te_2$ sample at 300 K, 473 K, and 673 K to investigate the phase transformations. The results, shown in Figure 4, indicate reversible phase transitions following the sequence orthorhombic ↔ tetragonal ↔ hexagonal phases (see XRD data in Figure S2 for 5-40 2theta range and in Figure S3 for the orthorhombic deformation of the tetragonal unit cell). The pattern obtained at 673 K could not be indexed with the cubic unit cell and lattice parameters reported by Stevels et al.[49]. However, the pattern was successfully indexed by considering a hexagonal unit cell with lattice parameters a = 7.2886 Å and c = 7.855 Å.

Phase Analysis. The EDX elemental mapping of $Cu_{2.8}Te_2$ indicates homogenous distribution of Cu and Te throughout the microstructure (Figure S4). Further EDX measurements of the samples were carried out at 6 different randomly chosen spots. These analyses reveal that the actual chemical compositions of the samples match the nominal ones (Table S3). More accurate compositions were obtained from WDS analysis by averaging 10 measurement

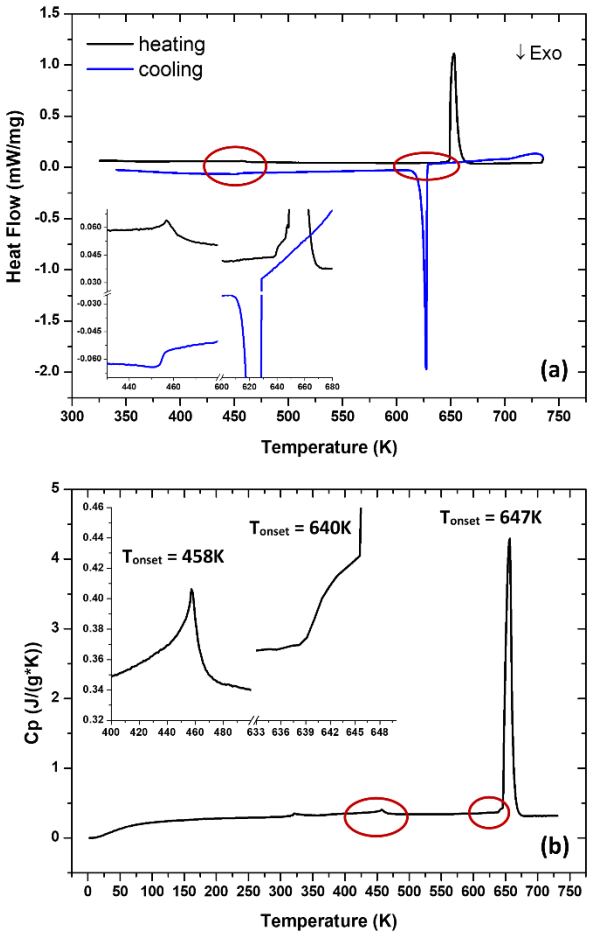

Figure 6. a) DSC thermogram of $Cu_{2.9}Te_2$ (scanning rate 10 K min^{-1}) showing reversible phase transitions at 458 K, 640 K and 647 K b) The Cp data of $Cu_{2.9}Te_2$. The inset graphs show corresponding red marked phase transition regions.

data points (Table S4 and Figure S5). The Cu content slightly increases with increasing the Cu content in the nominal composition; $Cu_{2.83(1)}Te_2$ (for $Cu_{2.8}Te_2$) and $Cu_{2.84(1)}Te_2$ (for $Cu_{2.9}Te_2$). These results are consistent with the existence of a small phase range for this material (Figure S1). Based on the reported binary phase diagram, the rickardite phase range was estimated to extend from x = 0 up to 0.18 in $Cu_{3-x}Te_2$[40].

Optical micrographs show strong orientation contrast of the target phase in polarized light (Figure 5). The microstructure is formed by primary grains of irregular shape that contain fine, lamellar domains. The shape and the very regular orientation of the domains strongly indicate a solid-state formation of the targeted phase during sample preparation. The very fine lamellae may originate from a polymorphic phase transformation from the primary high-temperature phase. Needle-like domains are generally consequences of a peritectoid decomposition of minor portions of the high-temperature phase. The grain size of the

samples varies significantly between 10 and 200 μm. A network of needle-like grains is observed within much larger grains.

The DSC thermogram (Figure 6a) indicates that $Cu_{2.9}Te_2$ undergoes at least three phase transitions at around 458 K, 640 K, and 647 K. These transitions are similar to those reported by Stevels and Wiegers at slightly lower temperatures of 413 K, 623 K and 633 K[49]. The first transition was described as a second-order phase transition corresponding to a change in the lattice symmetry from orthorhombic to tetragonal. The shoulder observed at 640 K near the main endothermic peak at 647 K was discussed in the context of tetragonal-to-rhombohedral and rhombohedral-to-fcc phase transitions[49]. Our results do not support the presence of a high-temperature cubic phase up to 733 K. The exothermic peaks appearing in the cooling cycle indicates that the phase transitions are reversible. In the DSC diagram of $Cu_{2.8}Te_2$ (Figure S6 and S7), four endothermic (at 460 K, 623 K, 650 K and 691K) and three exothermic peaks were observed on heating and cooling cycles, respectively. The first and third peaks are similar to the ones observed for $Cu_{2.9}Te_2$. The second endothermic peak is rather sharp and occurs at a distinctly lower temperature than the copper excess phase (623 K vs 640 K). The additional endothermic peak at 691 K coincides with the incongruent melting temperature of CuTe by the reaction: CuTe → M (high T cubic phase) + L (Liquid) [46].

The temperature dependence of the isobaric specific heat C_p of the $Cu_{2.9}Te_2$ sample is shown in Figure 6b. Only weak variations in the Cp values were observed between this sample and the stoichiometric sample $Cu_{2.8}Te_2$ (Figure S7). The low-temperature data of $Cu_{2.9}Te_2$ follows the free-electron formula $C_p/T = \gamma + \beta T^2$ below about 4.5 K. A fit of the data according to this relation yields an electron contribution γ of 10.3 mJ mol^{-1} K^{-2}, confirming a finite density of states at the Fermi level in the LT phase in agreement with the metallic behavior of this compound (see below). The β parameter of 2.85 mJ mol^{-1} K^{-4}, linked to the phonon contribution, corresponds to a Debye temperature of 200 K. At room temperature, C_p reaches a value of about 323 J mol^{-1} K^{-1}, which exceeds the Dulong-Petit limit of 300 J mol^{-1} K^{-1}. Upon further warming up to 733 K (Figure 6b), the two transitions evidenced by the XRD data give rise to two lambda-shaped anomalies at 458 and 647 K, in good agreement with the transport data. While the small amplitude of the first transition is in agreement with its weak fingerprints in the electronic data, the amplitude for the transition at 467 K is significantly larger, akin to that observed in SnSe[54, 55] near 800 K or in various argyrodite ionic conductors[56, 57]. An additional shoulder, close to the second phase transition temperature, is also visible at 640 K which might correspond to the onset of the structural reordering.

Electronic Transport Properties. The temperature dependences of the electrical resistivity, ρ and thermopower, α of $Cu_{2.9}Te_2$ sample are shown in Figure 7a and 7b, respectively. $Cu_{2.9}Te_2$ shows very low ρ values, indicative of a metallic behavior, that weakly increase with increasing temperature up to 650 K. Consistent with this degenerate nature, the α values remain below 10 μV. K^{-1} up to about 600

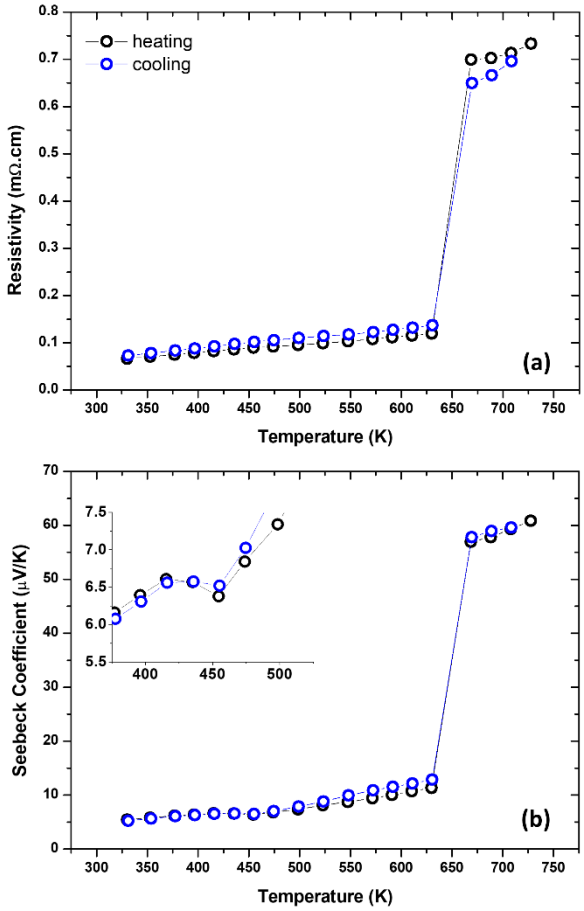

Figure 7. a) Electrical resistivity and b) Seebeck coefficient of $Cu_{2.9}Te_2$ as a function of temperature showing metallic behavior with a strong transition at 650 K and comparatively minor change at 450 K (see inset figure in (b)).

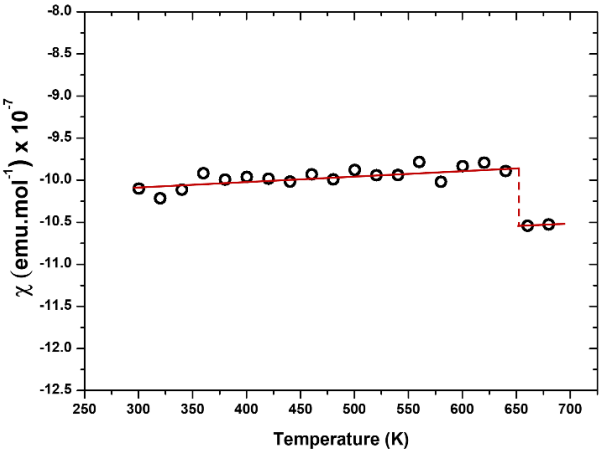

Figure 8. Temperature dependence of the magnetic susceptibility, χ of $Cu_{2.9}Te_2$ showing a small change at 650 K.

K. The shallow dip observed near 450 K corresponds to the first structural transition, the influence of which on the electrical properties remains nevertheless weak. At low temperatures, α(T) shows a broad maximum reached near 50 K likely due to a phonon drag contribution superimposed to the diffusive term that dominates above 100 K (Figure S8). The positive α values over the entire temperature range are indicative of holes as the dominant charge carriers. In contrast to the smooth variations in ρ and α with temperature up to about 600 K, a sudden increase in both properties is observed above 650 K. This temperature closely corresponds to the HT structural transition evidenced by XRD and DSC. Additional measurements performed upon heating and cooling across this second high-temperature transition did not evidence any hysteretic behavior to within experimental uncertainty (Figure S9, S10, and S11), in agreement with the reversible nature of this phase transition. All these traits remain similar in stoichiometric $Cu_{2.8}Te_2$, showing that both transitions are not sensitive to the Cu stoichiometry (Figure S9).

The nearly sevenfold and sixfold increase in ρ and α, respectively, observed above 650 K further suggests a metal-insulator-like transition. A removal of the density of states at the chemical potential induced by this transition, possibly leading to a full band gap opening, is supported by measurements of the magnetic susceptibility, χ (Figure 8). The negative χ values measured below the transition temperature decrease at higher temperatures. This variation is consistent with a decrease in the Pauli contribution that originates from the free charge carriers and hence, with at least a partial removal of the electronic density of states. However, whether or not a complete band gap opens in the high-temperature phase will require electronic band structure calculations.

One interesting aspect of the transport in this compound is the negative sign of the Hall response, which is opposite to that of α. The magnitude of the Hall coefficients corresponds to a large concentration of electron-like carriers on the order of 3×10^{22} cm^{-3} at 300 K, which is consistent with the degenerate behavior of this compound. The opposite signs of α and the Hall coefficient R_H in this metallic compound bears strong resemblance with what is observed in the alkali metal Li and the noble metals Cu, Ag and Au for which, the positive sign of α is a long-standing issue which is still yet to be fully understood[58].

Mainly three classes of scenarios have been advanced to reconcile both observations. A first class relates this sign change to peculiarities in Fermi surface topology, the distortion of which close to the Brillouin zone boundaries yielding both electron-like and hole-like curvatures[59], with the extreme case of direction-dependent sign of α in layered-like compounds dubbed as goniopolar materials[60]. The second class gathers models in which a strong energy dependence of electron-phonon interactions around the Fermi energy plays a central role[61]. A third possibility has been demonstrated in the specific case of Li for which, the positive sign of α originates from the energy dependence of the electron lifetime due to strong deviations in the electronic density of states around the Fermi energy from the free-electron model, with little influence of the electron-phonon coupling[62]. Determining into which class $Cu_{2.9}Te_2$ falls will require detailed electronic band structure and Fermi surface calculations.

Thermal transport. The temperature dependence of the total thermal conductivity κ at high-temperature is shown in Figure 9, while the low-temperature data are shown in Figure S8c. Below 300 K, κ rapidly increases with increasing temperature, reaching a value of about 13 $W\,m^{-1}\,K^{-1}$ at 150 K. Above this temperature, κ slowly decreases upon further warming to room temperature. The temperature dependence of κ is characteristic of crystalline solids with a dielectric maximum at low temperatures followed by a smooth decrease stemming from Umklapp scattering processes (Figure S8c). At higher temperatures, the first phase transition near 460 K is likely at the origin of the dip observed around this temperature. While the influence of this first transition on the thermal transport remains mild, the second phase transition observed in the Cp data give rise to a sharp drop in the κ values. Upon crossing this structural transition at 647 K, κ drops from 10.0 $W\,m^{-1}\,K^{-1}$ at 625 K to only 2.3 $W\,m^{-1}\,K^{-1}$ above 650 K. Of note, unlike ρ and α, a weak hysteretic behavior was observed upon warming above the second phase transition temperature a second time (Figure S11b). These variations might be related to a change in the grain size or in the microstructure.

The influence of structural phase transitions on the specific heat and thermal diffusivity has been discussed in prior studies on Zn_4Sb_3 at low temperatures and on binary Cu- and Ag-based chalcogenides that undergo transitions between 350 and 460 K[63, 64]. While the influence of structural phase transitions on C_p can be directly probed experimentally, how impacted is the thermal diffusivity across such a transition remains a delicate problem that can have a significant impact on the estimation of the κ values and, hence, of the zT values. In particular, the usually observed

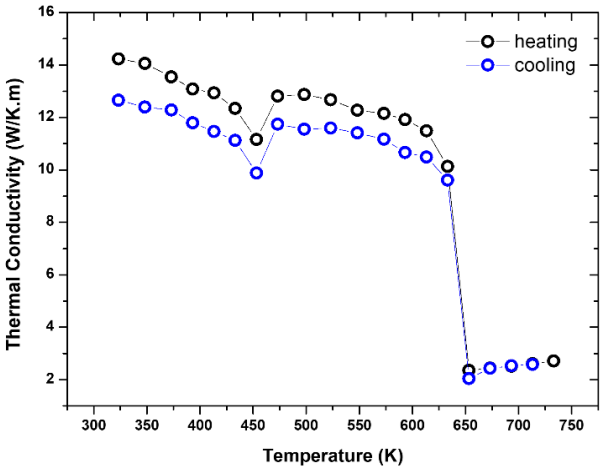

Figure 9. Thermal conductivity of $Cu_{2.9}Te_2$ showing effects of transitions at 450 K and 650 K.

dramatic decrease in the thermal diffusivity across the transition temperature may not reflect the intrinsic thermal transport of the material. In the case of $Cu_{2.8}Te_2$ and $Cu_{2.9}Te_2$, the possible gap opening induced by the structural transition near 650 K may also be at the origin of the strong decrease in the diffusivity data. The C_p values, that peak near this temperature, have been estimated following the method widely used in prior studies, as shown in Figure S7. Most importantly, the strongly increasing C_p values reflecting the extra energy required to transit towards the high-temperature phase were not considered. As suggested in prior studies, the impact of such a transition on the thermal diffusivity data can be qualitatively investigated by determining the speed of the transition, reflected by the shift in the peak temperature in the C_p data upon varying the heating rate. While fast transitions will strongly lower the thermal diffusivity values, slower transitions will lead to smooth variations of the thermal transport across the transition. To determine into which category the present compounds fall, we have measured the C_p data of $Cu_{2.9}Te_2$ with a heating rate of 20 K min^{-1}, that is, twice as high as the measurements shown in Figure 6. The result evidence significant shifts in the peak temperature characterizing both transitions (6 and 10 K for the first and second transition, respectively), indicative of slow transitions (Figure S12). This characteristic suggests that both transitions are smooth and hence, are not expected to dramatically alter the thermal properties. The weak yet discernible fingerprint of the first phase transition at 450 K on the thermal transport data supports this conclusion. Hence, the strong drop observed in the κ values near 650 K can be mainly attributed to the electronic metal-insulator-like transition, which removes a large fraction of the electronic thermal conductivity, rather than to an artificial decrease in the thermal diffusivity due to the phase transition.

The strong metallic character of $Cu_{2.9}Te_2$ implies that a large fraction of κ below 650 K is due to the electronic contribution κ_e. Thus, the significant reduction in κ is consistent with the metal-insulator transition observed in the electronic and magnetic properties. The substantial increase in ρ that accompanies this transition results in a drop in κ_e according to the Wiedemann-Franz (WF) law $\kappa_e = LT/\rho$ where L is the Lorenz number. Further disentangling the electronic and lattice contributions to κ is, however, challenging in the present case. Despite the strongly degenerate behavior of $Cu_{2.9}Te_2$, taking the corresponding degenerate limit for L, that is, $L_0 = 2.44\times10^{-8}$ V^2 K^{-2}, yields κ_e values that largely exceeds κ above 35 K. The deviations of L from this universal limit suggest differing electrical and thermal relaxation times due to the presence of inelastic electron-phonon and electron-electron scattering processes that significantly lower L values. The large deviations from L_0 can be estimated by assuming that above the second phase transition κ_e is negligible compared to the lattice contribution κ_L due to the strong increase in ρ. If we further assume that κ_L is equivalent in both the LT and HT phases, the κ_L value measured at 650 K can be used to estimate κ_e at 600 K and hence, L. This analysis yields a L value of 1.53×10^{-8} V^2 K^{-2}, which mirrors the low values usually determined in doped semiconductors above room temperature and unexpected result for such metallic material. The obtained low L value suggests that inelastic scattering events dominate the scattering mechanisms in this compound. Similar results were reported for some other complex metallic structures with unusually low Lorenz number [65, 66].

Thermoelectric figure of merit. Figure 10 shows the temperature dependence of the dimensionless thermoelectric figure of merit, zT, of $Cu_{2.9}Te_2$ (see Figure S8 for $Cu_{2.8}Te_2$). The strong metallic character of the transport properties below 650 K results in very small values. However, the metal-insulator transition undergone by $Cu_{2.9}Te_2$ results in a steep rise in the zT values above this temperature, with a peak value of around 0.14 achieved at 673 K, due to the concomitant increase in the power factor α^2/ρ and the drop in the thermal conductivity, κ.

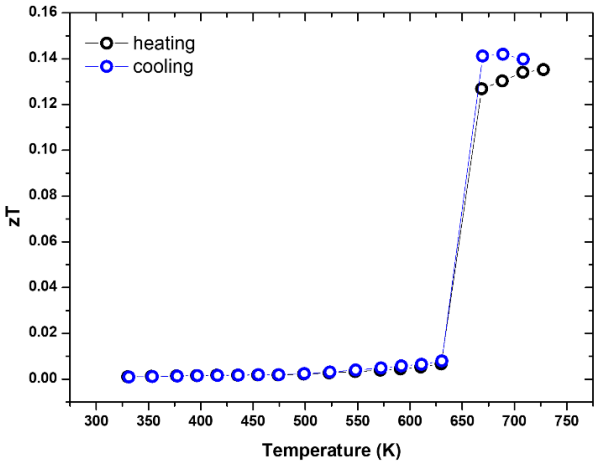

Figure 10. Temperature dependence of zT curves of $Cu_{2.9}Te_2$ upon heating and cooling showing rapid increase in zT above the transition at 650 K.

CONCLUSIONS

Synthetic polycrystalline rickardite samples with $Cu_{3-x}Te_2$ (x = 0.1 and 0.2) compositions were successfully synthesized by a direct solid-state reaction. These samples undergo several reversible phase transitions at 458 K, 640 K, and 647 K based on a combined analysis of high-temperature X-ray diffraction, differential scanning calorimetry and specific heat measurements. The electronic and thermal transport properties measured over a broad range of temperatures (5 – 673 K) display signatures of these phase transitions with notably a crossover from metallic-like to semiconducting-like properties at around 650 K. A peak zT ~ 0.14 is obtained at 733 K thanks to moderate power factor and low thermal conductivity attained in the high-temperature phase. As a phase-changing material, the current

study on rickardite mineral may provide insightful strategies for designing functional products e.g., in waste-heat harvesting, and photovoltaic systems.

ASSOCIATED CONTENT

Supporting Information

The Supporting Information is available free of charge at http://pubs.acs.org/.....

The binary phase diagram of Cu-Te; crystallographic data of $Cu_{2.9}Te_2$ atomic coordinates, displacement parameters and site occupancy factor (SOF) of $Cu_{2.9}Te_2$; the back-scattered electron image and elemental mapping of $Cu_{2.8}Te_2$; EDX analysis results of $Cu_{2.8}Te_2$ and $Cu_{2.9}Te_2$; SEM images of $Cu_{2.8}Te_2$ and $Cu_{2.9}Te_2$ for WDS analysis; the WDS analysis results of $Cu_{2.8}Te_2$ and $Cu_{2.9}Te_2$; DSC thermogram of $Cu_{2.8}Te_2$; the C_p of $Cu_{2.8}Te_2$ and $Cu_{2.9}Te_2$; low temperature electronic and thermal transport data of $Cu_{2.8}Te_2$; the C_p of $Cu_{2.9}Te_2$ with heating rates of 10 K/min and 20 K/min; comparison of the electronic and thermal transport data of $Cu_{2.8}Te_2$ and $Cu_{2.9}Te_2$; resistivity and Seebeck coefficient of $Cu_{2.9}Te_2$ with the second cycle performed to the temperature 573 K; the repeated thermal conductivity measurements of $Cu_{2.9}Te_2$ to the temperature of 573 K and 673 K.

AUTHOR INFORMATION

Corresponding Author

Umut Aydemir - Department of Chemistry, Koç University, Sariyer, Istanbul-34450, Turkey; Koç University Boron and Advanced Materials Application and Research Center (KUBAM), Sariyer, Istanbul-34450, Turkey; orcid.org/0000-0003-1164-1973

Email: uaydemir@ku.edu.tr

Authors

Mujde Yahyaoglu - Graduate School of Sciences and Engineering, Koç University, Sariyer, Istanbul-34450, Turkey; Koç University Boron and Advanced Materials Application and Research Center (KUBAM), Sariyer, Istanbul-34450, Turkey; orcid.org/0000-0001-9098-2869

Melis Ozen - Graduate School of Sciences and Engineering, Koç University, Sariyer, Istanbul-34450, Turkey; Koç University Boron and Advanced Materials Application and Research Center (KUBAM), Sariyer, Istanbul-34450, Turkey; orcid.org/0000-0003-3498-3941

Yurii Prots - Max-Planck-Institut für Chemische Physik fester Stoffe, Dresden-01187, Germany; orcid.org/0000-0002-7418-9892

Oussama El Hamouli - Institut Jean Lamour, Université de Lorraine, Nancy Cedex-54011, France;

Vahe Tshitoyan - Energy Technologies Area, Lawrence Berkeley National Lab, Berkeley, CA-94720, USA;

Huiwen Ji - Energy Technologies Area, Lawrence Berkeley National Lab, Berkeley, CA-94720, USA;

Ulrich Burkhardt - Max-Planck-Institut für Chemische Physik fester Stoffe, Dresden-01187, Germany;

Bertrand Lenoir - Institut Jean Lamour, Université de Lorraine, Nancy Cedex-54011, France; orcid.org/0000-0001-9631-4925

G. Jeffrey Snyder - Department of Materials Science and Engineering, Northwestern University, Evanston, IL-60208, USA; orcid.org/0000-0003-1414-8682

Anubhav Jain - Energy Technologies Area, Lawrence Berkeley National Lab, Berkeley, CA-94720, USA;

Christophe Candolfi - Institut Jean Lamour, Université de Lorraine, Nancy Cedex-54011, France; orcid.org/0000-0002-1248-5354

Author Contributions

The manuscript was written through the contributions of all authors. All authors have given approval to the final version of the manuscript.

Notes

The authors declare no competing financial interest.

ACKNOWLEDGMENT

UA greatly acknowledges the financial support of the Science Academy through the 2018 Science Academy's Young Scientist Award (BAGEP). AJ acknowledges funding from Toyota Research Institute through the Accelerated Materials Design and Discovery program. Lawrence Berkeley National Laboratory is funded by the DOE under award DE-AC02-05CH11231. We would like to thank Dr. Lev Akselrud from Ivan Franko National University of Lviv for fruitful discussions on crystal structure determination and Dr. Christos D. Malliakas from Integrated Molecular Structure Education and Research Center (IMSERC) at Northwestern University for the high-temperature XRD measurements.

REFERENCES

1. He, J.; Tritt, T. M., Advances in thermoelectric materials research: Looking back and moving forward. *Science* **2017,** *357* (6358).
2. Slack, G. A., New Materials and Performance Limits for Thermoelectric Cooling. In: Rowe D M (eds.). *CRC Handbook of Thermoelectrics* **1995**, 407-440.
3. Qiu, P.; Shi, X.; Chen, L., Cu-based thermoelectric materials. *Energy Storage Materials* **2016,** *3*, 85-97.
4. Wei, T.-R.; Qin, Y.; Deng, T.; Song, Q.; Jiang, B.; Liu, R.; Qiu, P.; Shi, X.; Chen, L., Copper chalcogenide thermoelectric materials. *Science China Materials* **2019,** *62* (1), 8-24.
5. Liu, H.; Shi, X.; Xu, F.; Zhang, L.; Zhang, W.; Chen, L.; Li, Q.; Uher, C.; Day, T.; Snyder, G. J., Copper ion liquid-like thermoelectrics. *Nature materials* **2012,** *11* (5), 422-425.
6. He, Y.; Day, T.; Zhang, T.; Liu, H.; Shi, X.; Chen, L.; Snyder, G. J., High thermoelectric performance in non-toxic earth-abundant copper sulfide. *Advanced Materials* **2014,** *26* (23), 3974-3978.
7. He, Y.; Zhang, T.; Shi, X.; Wei, S.-H.; Chen, L., High thermoelectric performance in copper telluride. *NPG Asia Materials* **2015,** *7* (8), e210-e210.

8. He, Y.; Lu, P.; Shi, X.; Xu, F.; Zhang, T.; Snyder, G. J.; Uher, C.; Chen, L., Ultrahigh thermoelectric performance in mosaic crystals. *Advanced Materials* **2015,** *27* (24), 3639-3644.

9. Zhao, L.; Wang, X.; Fei, F. Y.; Wang, J.; Cheng, Z.; Dou, S.; Wang, J.; Snyder, G. J., High thermoelectric and mechanical performance in highly dense Cu 2– x S bulks prepared by a melt-solidification technique. *Journal of Materials Chemistry A* **2015,** *3* (18), 9432-9437.

10. Islam, S. M. K. N.; Li, M.; Aydemir, U.; Shi, X.; Chen, L.; Snyder, G. J.; Wang, X., Giant enhancement of the figure-of-merit over a broad temperature range in nano-boron incorporated Cu 2 Se. *Journal of Materials Chemistry A* **2018,** *6* (38), 18409-18416.

11. Li, M.; Islam, S. M. K. N.; Yahyaoglu, M.; Pan, D.; Shi, X.; Chen, L.; Aydemir, U.; Wang, X., Ultrahigh figure-of-merit of Cu2Se incorporated with carbon coated boron nanoparticles. *InfoMat* **2019,** *1* (1), 108-115.

12. Zhao, K.; Blichfeld, A. B.; Chen, H.; Song, Q.; Zhang, T.; Zhu, C.; Ren, D.; Hanus, R.; Qiu, P.; Iversen, B. B., Enhanced Thermoelectric Performance through Tuning Bonding Energy in Cu2Se1–x S x Liquid-like Materials. *Chemistry of Materials* **2017,** *29* (15), 6367-6377.

13. Gahtori, B.; Bathula, S.; Tyagi, K.; Jayasimhadri, M.; Srivastava, A.; Singh, S.; Budhani, R.; Dhar, A., Giant enhancement in thermoelectric performance of copper selenide by incorporation of different nanoscale dimensional defect features. *Nano Energy* **2015,** *13*, 36-46.

14. Nunna, R.; Qiu, P.; Yin, M.; Chen, H.; Hanus, R.; Song, Q.; Zhang, T.; Chou, M.-Y.; Agne, M. T.; He, J., Ultrahigh thermoelectric performance in Cu 2 Se-based hybrid materials with highly dispersed molecular CNTs. *Energy & Environmental Science* **2017,** *10* (9), 1928-1935.

15. Olvera, A.; Moroz, N.; Sahoo, P.; Ren, P.; Bailey, T.; Page, A.; Uher, C.; Poudeu, P., Partial indium solubility induces chemical stability and colossal thermoelectric figure of merit in Cu 2 Se. *Energy & Environmental Science* **2017,** *10* (7), 1668-1676.

16. Ge, Z. H.; Liu, X.; Feng, D.; Lin, J.; He, J., High-Performance Thermoelectricity in Nanostructured Earth-Abundant Copper Sulfides Bulk Materials. *Advanced Energy Materials* **2016,** *6* (16), 1600607.

17. Jiang, B.; Qiu, P.; Eikeland, E.; Chen, H.; Song, Q.; Ren, D.; Zhang, T.; Yang, J.; Iversen, B. B.; Shi, X., Cu 8 GeSe 6-based thermoelectric materials with an argyrodite structure. *Journal of Materials Chemistry C* **2017,** *5* (4), 943-952.

18. Qiu, P.; Zhang, T.; Qiu, Y.; Shi, X.; Chen, L., Sulfide bornite thermoelectric material: a natural mineral with ultralow thermal conductivity. *Energy & Environmental Science* **2014,** *7* (12), 4000-4006.

19. Weldert, K. S.; Zeier, W. G.; Day, T. W.; Panthöfer, M.; Snyder, G. J.; Tremel, W., Thermoelectric transport in Cu7PSe6 with high copper ionic mobility. *Journal of the American Chemical Society* **2014,** *136* (34), 12035-12040.

20. Bhattacharya, S.; Basu, R.; Bhatt, R.; Pitale, S.; Singh, A.; Aswal, D.; Gupta, S.; Navaneethan, M.; Hayakawa, Y., CuCrSe 2: a high performance phonon glass and electron crystal thermoelectric material. *Journal of Materials Chemistry A* **2013,** *1* (37), 11289-11294.

21. Ishiwata, S.; Shiomi, Y.; Lee, J.; Bahramy, M.; Suzuki, T.; Uchida, M.; Arita, R.; Taguchi, Y.; Tokura, Y., Extremely high electron mobility in a phonon-glass semimetal. *Nature materials* **2013,** *12* (6), 512-517.

22. Han, C.-G.; Zhang, B.-P.; Ge, Z.-H.; Zhang, L.-J.; Liu, Y.-C., Thermoelectric properties of p-type semiconductors copper chromium disulfide CuCrS 2+ x. *Journal of Materials Science* **2013,** *48* (11), 4081-4087.

23. Plirdpring, T.; Kurosaki, K.; Kosuga, A.; Day, T.; Firdosy, S.; Ravi, V.; Snyder, G. J.; Harnwunggmoung, A.; Sugahara, T.; Ohishi, Y., Chalcopyrite CuGaTe2: A High-Efficiency Bulk Thermoelectric Material. *Advanced Materials* **2012,** *24* (27), 3622-3626.

24. Liu, R.; Xi, L.; Liu, H.; Shi, X.; Zhang, W.; Chen, L., Ternary compound CuInTe 2: a promising thermoelectric material with diamond-like structure. *Chemical Communications* **2012,** *48* (32), 3818-3820.

25. Liu, Y.; García, G.; Ortega, S.; Cadavid, D.; Palacios, P.; Lu, J.; Ibáñez, M.; Xi, L.; De Roo, J.; López, A. M., Solution-based synthesis and processing of Sn-and Bi-doped Cu 3 SbSe 4 nanocrystals, nanomaterials and ring-shaped thermoelectric generators. *Journal of materials chemistry A* **2017,** *5* (6), 2592-2602.

26. Skoug, E. J.; Cain, J. D.; Morelli, D. T., High thermoelectric figure of merit in the Cu3SbSe4-Cu3SbS4 solid solution. *Applied Physics Letters* **2011,** *98* (26), 261911.

27. Shi, X.; Xi, L.; Fan, J.; Zhang, W.; Chen, L., Cu– Se bond network and thermoelectric compounds with complex diamondlike structure. *Chemistry of Materials* **2010,** *22* (22), 6029-6031.

28. Lin, H.; Chen, H.; Shen, J. N.; Chen, L.; Wu, L. M., Chemical modification and energetically favorable atomic disorder of a layered thermoelectric material TmCuTe2 leading to high performance. *Chemistry–A European Journal* **2014,** *20* (47), 15401-15408.

29. Gulay, L.; Daszkiewicz, M.; Shemet, V. Y., Crystal structure of~ RCu3S3 and~ RCuTe2 (R= Gd–Lu) compounds. *Journal of Solid State Chemistry* **2012,** *186*, 142-148.

30. Oudah, M.; Kleinke, K. M.; Kleinke, H., Thermoelectric properties of the quaternary chalcogenides BaCu5. 9STe6 and BaCu5. 9SeTe6. *Inorganic chemistry* **2015,** *54* (3), 845-849.

31. Zhao, L.-D.; He, J.; Berardan, D.; Lin, Y.; Li, J.-F.; Nan, C.-W.; Dragoe, N., BiCuSeO oxyselenides: new promising thermoelectric materials. *Energy & Environmental Science* **2014,** *7* (9), 2900-2924.

32. Lan, J. L.; Liu, Y. C.; Zhan, B.; Lin, Y. H.; Zhang, B.; Yuan, X.; Zhang, W.; Xu, W.; Nan, C. W., Enhanced thermoelectric properties of Pb-doped BiCuSeO ceramics. *Advanced Materials* **2013,** *25* (36), 5086-5090.

33. Li, F.; Wei, T.-R.; Kang, F.; Li, J.-F., Enhanced thermoelectric performance of Ca-doped BiCuSeO in a wide temperature range. *Journal of Materials Chemistry A* **2013,** *1* (38), 11942-11949.

34. Aydemir, U.; Pöhls, J.-H.; Zhu, H.; Hautier, G.; Bajaj, S.; Gibbs, Z. M.; Chen, W.; Li, G.; Ohno, S.; Broberg, D., YCuTe 2: a member of a new class of thermoelectric materials with CuTe 4-based layered structure. *Journal of Materials Chemistry A* **2016,** *4* (7), 2461-2472.

35. Weston, L.; Tshitoyan, V.; Dagdelen, J.; Kononova, O.; Trewartha, A.; Persson, K. A.; Ceder, G.; Jain, A., Named Entity Recognition and Normalization Applied to Large-Scale Information Extraction from the Materials Science Literature. *Journal of chemical information and modeling* **2019,** *59* (9), 3692-3702.

36. Tshitoyan, V.; Dagdelen, J.; Weston, L.; Dunn, A.; Rong, Z.; Kononova, O.; Persson, K. A.; Ceder, G.; Jain, A., Unsupervised word embeddings capture latent knowledge from materials science literature. *Nature* **2019,** *571* (7763), 95-98.

37. Ricci, F.; Chen, W.; Aydemir, U.; Snyder, G. J.; Rignanese, G.-M.; Jain, A.; Hautier, G., An ab initio electronic

transport database for inorganic materials. *Scientific data* **2017,** *4*, 170085.

38. Gaultois, M. W.; Sparks, T. D.; Borg, C. K.; Seshadri, R.; Bonificio, W. D.; Clarke, D. R., Data-driven review of thermoelectric materials: performance and resource considerations. *Chemistry of Materials* **2013,** *25* (15), 2911-2920.

39. Patzak, I., Uber die struktur und die lage der phasen im system kupfer-tellur. *Zeitschrift für Metallkunde* **1956,** *47* (6), 418-420.

40. Forman, S. A.; Peacock, M., Crystal structure of rickardite, Cu4–Te2. *American Mineralogist: Journal of Earth and Planetary Materials* **1949,** *34* (5-6), 441-451.

41. Jia, G.; Wang, C.; Yang, P.; Liu, J.; Zhang, W.; Li, R.; Zhang, S.; Du, J., Sulfur-free synthesis of size tunable rickardite (Cu3– x Te2) spheroids and planar squares. *Royal Society open science* **2019,** *6* (2), 181602.

42. Pandey, J.; Mukherjee, S.; Rawat, D.; Athar, S.; Rana, K. S.; Mallik, R. C.; Soni, A., Raman Spectroscopy Study of Phonon Liquid Electron Crystal in Copper Deficient Superionic Thermoelectric Cu2–x Te. *ACS Applied Energy Materials* **2020,** *3* (3), 2175-2181.

43. Rajkumar, R.; Nedunchezhian, A. A.; Sidharth, D.; Rajasekaran, P.; Arivanandhan, M.; Jayavel, R.; Anbalagan, G., Effect of sintering temperatures on mixed phases and thermoelectric properties of nanostructured copper telluride. *Journal of Alloys and Compounds* **2020**, 155276.

44. Bouyrie, Y.; Ohorodniichuk, V.; Sassi, S.; Masschelein, P.; Dauscher, A.; Candolfi, C.; Lenoir, B., High-Temperature Transport Properties of Colusite Cu 24 T 2 V 2 Ge 6 S 32 (T= Ni, Co). *Journal of Electronic Materials* **2017,** *46* (5), 2684-2690.

45. Lu, X.; Morelli, D. T., Natural mineral tetrahedrite as a direct source of thermoelectric materials. *Physical Chemistry Chemical Physics* **2013,** *15* (16), 5762-5766.

46. Pashinkin, A.; Fedorov, V., Phase equilibria in the Cu–Te system. *Inorganic Materials* **2003,** *39* (6), 539-554.

47. Akselrud, L.; Grin, Yu., WinCSD: software package for crystallographic calculations (Version 4). *Journal of Applied Crystallography* **2014,** *47* (2), 803-805.

48. Thompson, R., The telluride minerals and their occurrence in Canada. *American Mineralogist: Journal of Earth and Planetary Materials* **1949,** *34* (5-6), 341-382.

49. Stevels, A.; Wiegers, G., Phase transitions in copper chalcogenides II. The tellurides Cu3-x Te2 and CuTe. *Recueil des Travaux Chimiques des Pays-Bas* **1971,** *90* (4), 352-359.

50. Elander, M.; Hägg, G.; Westgren, A., *The Crystal Structure of Cu2Sb and Fe2As*. Almqvist & Wiksell: 1935, P 1-6.

51. Rodriguez, E. E.; Zavalij, P.; Hsieh, P.-Y.; Green, M. A., Iodine as an Oxidant in the Topotactic Deintercalation of Interstitial Iron in Fe1+ x Te. *Journal of the American Chemical Society* **2010,** *132* (29), 10006-10008.

52. Ding, Y.; Wang, Y.; Ni, J., Electronic and magnetic properties of 3d transition-metal selenides from first principles. *Solid state communications* **2009,** *149* (13-14), 505-509.

53. Huang, T.-W.; Chen, T.-K.; Yeh, K.-W.; Ke, C.-T.; Chen, C. L.; Huang, Y.-L.; Hsu, F.-C.; Wu, M.-K.; Wu, P. M.; Avdeev, M., Doping-driven structural phase transition and loss of superconductivity in M x Fe 1–x Se δ (M= Mn, Cu). *Physical Review B* **2010,** *82* (10), 104502.

54. Sassi, S.; Candolfi, C.; Vaney, J.-B.; Ohorodniichuk, V.; Masschelein, P.; Dauscher, A.; Lenoir, B., Assessment of the thermoelectric performance of polycrystalline p-type SnSe. *Applied Physics Letters* **2014,** *104* (21), 212105.

55. Bansal, D.; Hong, J.; Li, C. W.; May, A. F.; Porter, W.; Hu, M. Y.; Abernathy, D. L.; Delaire, O., Phonon anharmonicity and negative thermal expansion in SnSe. *Physical Review B* **2016,** *94* (5), 054307.

56. Kawaji, H.; Atake, T., Heat capacity measurement and thermodynamic study of Ag8GeTe6. *Solid state ionics* **1994,** *70*, 518-521.

57. Li, L.; Liu, Y.; Dai, J.; Hong, A.; Zeng, M.; Yan, Z.; Xu, J.; Zhang, D.; Shan, D.; Liu, S., High thermoelectric performance of superionic argyrodite compound Ag 8 SnSe 6. *Journal of Materials Chemistry C* **2016,** *4* (24), 5806-5813.

58. F. J. Blatt , P. A. S., C. L. Foiles and D. Greig, *Thermoelectric Power of Metals*. Plenum Press: New York, 1976, P 135-190.

59. Jones, H., The Thermoelectric Power of Monovalent Metals. *Proceedings of the Physical Society. Section A* **1955,** *68* (12), 1191.

60. He, B.; Wang, Y.; Arguilla, M. Q.; Cultrara, N. D.; Scudder, M. R.; Goldberger, J. E.; Windl, W.; Heremans, J. P., The Fermi surface geometrical origin of axis-dependent conduction polarity in layered materials. *Nature materials* **2019,** *18* (6), 568-572.

61. Robinson, J. E.; Dow, J. D., Electron-Phonon Interactions in Solid Alkali Metals. I. Scattering and Transport Coefficients. *Physical Review* **1968,** *171* (3), 815.

62. Xu, B.; Verstraete, M. J., First principles explanation of the positive Seebeck coefficient of lithium. *Physical review letters* **2014,** *112* (19), 196603.

63. Chen, H.; Yue, Z.; Ren, D.; Zeng, H.; Wei, T.; Zhao, K.; Yang, R.; Qiu, P.; Chen, L.; Shi, X., Thermal conductivity during phase transitions. *Advanced Materials* **2019,** *31* (6), 1806518.

64. Agne, M. T.; Voorhees, P. W.; Snyder, G. J., Phase transformation contributions to heat capacity and impact on thermal diffusivity, thermal conductivity, and thermoelectric performance. *Advanced Materials* **2019,** *31* (35), 1902980.

65. Kazem, N.; Zaikina, J. V.; Ohno, S.; Snyder, G. J.; Kauzlarich, S. M., Coinage-metal-stuffed Eu9Cd4Sb9: Metallic compounds with anomalous low thermal conductivities. *Chemistry of Materials* **2015,** *27* (21), 7508-7519.

66. Aydemir, U.; Zevalkink, A.; Ormeci, A.; Wang, H.; Ohno, S.; Bux, S.; Snyder, G. J., Thermoelectric properties of the Zintl phases Yb 5 M 2 Sb 6 (M= Al, Ga, In). *Dalton Transactions* **2015,** *44* (15), 6767-6774.

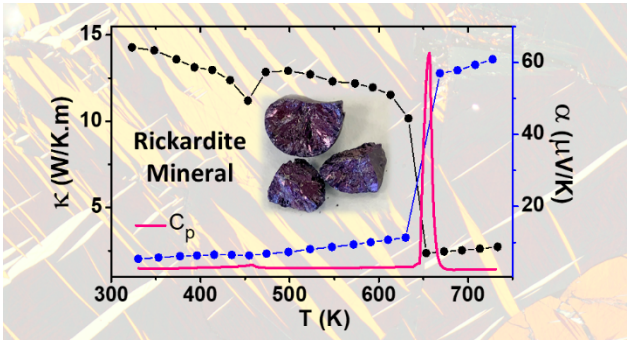
15
10
5
κ (W/K.m)
60
40
20
α (μV/K)
Rickardite
Mineral
Cp
300
400
500
600
700
T (K)

TOC Graphic